ELSEVIER

PII: S1359-8368(97)00004-8

Composites Part B **29B** (1998) 131–145

1359-8368/98/$19.00

Experiments and analysis of fiber fragmentation in single and multiple-fiber SiC/Ti-6Al-4V metal matrix composites

B. S. Majumdar[a], T. E. Matikas[b] and D. B. Miracle[c]
[a]*WL/MLLM, UES, Inc., 4401 Dayton-Xenia Road, Dayton, OH 45432, USA*
[b]*WL/MLLP, UDRI, Dayton, OH 45469, USA*
[c]*USAF Wright Laboratory Materials Directorate, Wright Patterson Air Force Base, OH 45433, USA*

Single-fiber and multiple-fiber single-ply fragmentation experiments were performed at room temperature on SiC/Ti-6Al-4V specimens, to understand interface shear failure under fragmentation conditions and to assess load-sharing behavior in longitudinally loaded composites. Tensile specimens were instrumented with two acoustic emission sensors and an extensometer to monitor the strain at which fiber breaks occurred. Following testing, the break locations were determined using a novel ultrasonic shear-wave back reflection (SBR) technique. Data analysis was performed using Curtin's exact fiber fragmentation model, wherein the *in situ* Weibull strength and Weibull modulus of the fiber, and the average shear stress under fragmentation conditions, were determined based on best fit with two essentially independent sets of data from the experiments, i.e. the breaking stress of the fibers, and the fragment length distribution. Results for the SCS-6/Ti-6Al-4V samples are presented in this paper, and they are compared with results from other SiC fibers in the same Ti-alloy matrix. The average shear stress from the fragmentation test was significantly higher than that obtained by push-out tests, and is explained on the basis of high radial clamping stress on the fiber in the immediate vicinity of a fiber break. Experiments were also performed on multi-fiber single-ply specimens. Comparison with the single-fiber results showed evidence of correlated fracture even for the relatively weak interface of the SCS-6 fiber. SBR image and macroscopic slip bands indicate that localized plasticity plays a dominant role in promoting correlated fiber fractures at room temperature, and the mechanism is outlined.

(Keywords: A. fibres; B. fragmentation; C. stress concentrations)

INTRODUCTION

It is generally well accepted that the fiber–matrix interface plays a critical role in the performance of fiber–reinforced metal matrix composites[1]. Diverse composite performance goals often impose interface property requirements that may be contradictory in nature. Thus, the composite strength and creep resistance in the transverse direction are improved by a stronger interface tensile (i.e. radial) strength, whereas a weak interface is generally desired for crack bridging under fatigue crack growth conditions under longitudinal loading. A recent review article provides a description of the issues involved[2]. As efforts are made to tailor the interface to satisfy conflicting property requirements, it is desirable to ensure that the interface characterization procedures not only replicate the important modes of interface failure (such as tensile or shear failure), but also that the test techniques simulate as much as possible the stress states under which the particular mode of failure occurs in actual application. Otherwise, the applicability of the test results for any specific application may become problematic or may require evaluation of a larger test matrix, because of the sensitivity of the interface failure conditions on the local stress states and associated additional damage modes and damage interactions. One example is the effect of radial clamping stress on shear failure of the interface under push-out loading[3,4], and another example is the influence of interface tangential shear failure on the normal separation of the interface under transverse loading[5,6].

This study is part of an overall effort to evaluate the influence of the interface on the longitudinal [0°] tensile behavior of unidirectional titanium matrix composites (TMCs), in the absence of a matrix crack. Under this type of loading, the interface becomes important only when there is a fiber break (see *Figure 1*), with the interface failure mode assumed as being primarily in shear. The effect of the fiber fracture is to impose additional loads on the neighboring fibers, which may either fail sympathetically if the stress concentration is high, or which may resist failing if the stress concentration is low, such that final failure of the composite is preceded by random failures of the fibers throughout the gage length of the sample. The former mode and sequence of fiber failures is

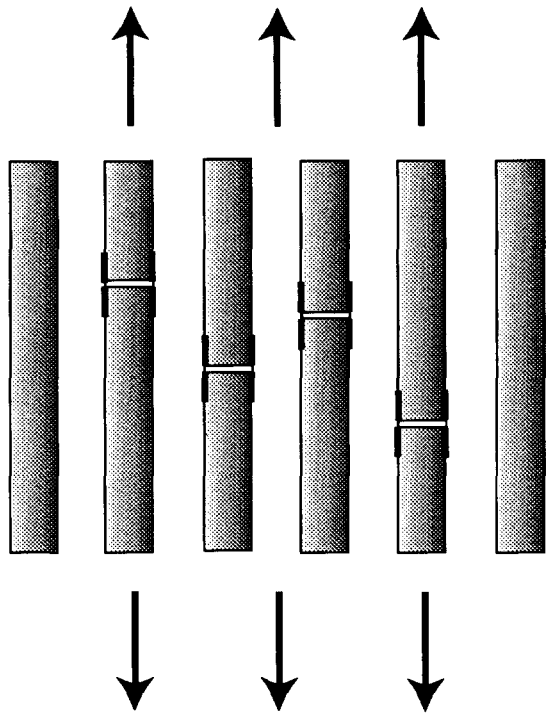

Figure 1 Sketch of a unidirectionally loaded composite without any matrix crack, illustrating that the interface becomes important when there is a fiber break

termed cumulative and the load sharing behavior is called local load sharing (LLS). The latter mode is termed noncumulative, and the load sharing behavior is called global load sharing (GLS).

From an interface characterization perspective, such that the data be useful in assessing load sharing behavior of the composite under longitudinal tension, the current understanding is that the test procedure must induce shear failure of the interface parallel to the fiber axis; perhaps there is an inherent assumption here regarding the interface failure mode and its influence on LLS *versus* GLS behavior. In any case, assuming that the understanding is correct, the shear mode of interface failure is most often characterized by the push-out test, which essentially involves push-out of fibers from a thin slice (~0.2–0.8 mm) of the composite. Recent observations and analysis[7–9] show that in these tests the interface failure occurs from the face away from the indenter, where the fiber–matrix interface next to the fiber end at the bottom surface experiences substantially less radial clamping stress (even radial tension, for sufficiently thin specimens) than the interface in the immediate vicinity of a fiber break in a longitudinally loaded sample. Consequently, the push-out test may not provide data that is relevant for the longitudinal tensile loading configuration that is of interest here.

The test technique that does appear to bear significant resemblance to the fiber fracture scenario is the single fiber fragmentation (SFF) test, and therefore this approach was selected for the current investigation. In order to preserve simplicity and continuity with past SFF test efforts[10,11], the interface failure was characterized in terms of a single shear parameter, τ. This parameter is often termed as the frictional sliding stress, but more appropriately it represents an average shear stress at the interface through which a broken fiber regains its load through elastic and/or relative fiber–matrix sliding displacements; the nomenclature 'frictional' derives from the assumed dominance of sliding displacements. The fiber fragmentation behavior was characterized in this work for the SiC/Ti-6Al-4V system, using SCS-6 fibers fabricated by Textron Specialty Metals. The results for the SCS-6 fiber are compared with those for a Trimarc fiber fabricated by Amercom, and for the uncoated SCS-0 fiber fabricated by Textron. The fibers were selected based on previous studies, which showed that the interface possessed tensile (normal) strengths that ranged from almost zero (for Trimarc) to about 380 MPa (for SCS-0), and average debond shear stresses (at peak load) ranging from 30 MPa to about 300 MPa under pushout conditions. The rationale was that this reasonably broad spectrum of interface properties would allow an assessment of the fragmentation test technique. In addition to the single-fiber fragmentation test, multiple-fiber fragmentation (MFF) experiments also were performed with multiple-fiber single-ply specimens, using the SCS-6 fibers. Comparison of those data with the single-fiber results allowed insight into the influence of the interface property on local *versus* global load sharing behavior.

There have only been a few attempts in the past to evaluate interface shear properties in MMCs using the SFF test[12,13]. On the other hand, the test is quite common for PMCs, and the most common data reduction procedure is to use the shear lag equation:

$$\tau = (\sigma d)/4\delta \tag{1}$$

to obtain an average shear strength of the interface, where τ is the average fiber–matrix interfacial shear stress, d is the fiber diameter, δ is the shear lag distance, and σ is the fiber stress. In the simple Kelly and Tyson formulation[10], σ is identified with an average fiber strength, and δ is identified with half the average fragment length, L_C, at fiber break saturation in the fiber fragmentation test. Since fiber strengths are generally statistical in nature, this requires an independent measurement of fiber strength (for a given fiber length), and then extrapolating it to the strength corresponding to the average fragment length at saturation. In addition, the procedure assumes that the *in situ* strength of the fibers in the composite remain the same as when fibers are tested independently, an assumption that may be violated in TMCs. Although the Kelly–Tyson formulation is simple, it totally neglects the evolution of fiber breaks and the distribution of fragment lengths, parameters that provide important understanding of the fiber fragmentation process. Furthermore, it does not provide a methodology to assess stress concentration effects in multiple fiber samples, such that the influence of the interface on LLS *versus* GLS can be evaluated.

In this work, we have used the analytical fiber fragmentation procedure of Curtin[14] to analyze the fragmentation data. As will be shown, the three parameters that

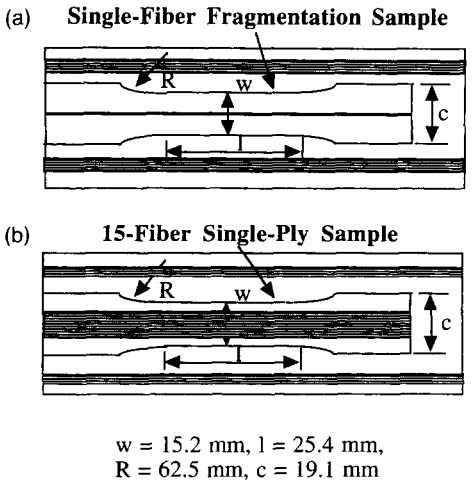

Figure 2 Sketch illustrating the specimen design in the fragmentation tests: (a) single-fiber, and (b) multiple fiber specimen

emerge from analysis of the data are: the *in situ* Weibull modulus (m) and Weibull strength (σ_0) of the fiber, and the average shear stress, τ, at the interface under sliding conditions. It will also be shown that the in situ Weibull modulus is a good indicator of stress concentration effects in multi-fiber specimens.

EXPERIMENTS

Single- and multi-fiber single-ply specimens were fabricated by hot pressing SiC fibers between two 115 × 32 × 0.38 mm Ti-6Al-4V sheets at 950°C under a pressure of approximately 40 MPa. Adequate fixtures and processing steps were utilized to ensure that there was complete consolidation with minimal residual defects at the interface. Tensile specimens were prepared by electric discharge machining, according to the dimensions sketched in *Figure 2*. Although the gage width is large for a single-fiber specimen, it was considered necessary for the multi-fiber specimens, so that fibers were well separated from the shoulders and ensured fiber failures in the gage section. More specifically, preliminary tests with narrower multi-fiber specimens revealed that even the small stress concentration associated with 62.5 mm shoulder radius could set up a chain of local fiber fractures, such that subsequent composite deformation was entirely localized in those regions rather than in the gage section. Three different fibers were utilized: SCS-6, SCS-0 and Trimarc, and only the results for the SCS-6 fiber are described in detail in this paper. Multiple-fiber specimens contained 15 fibers, and had a center-to-center distance of approximately 0.7 mm. Some specimens were prepared with 40 fibers at a spacing of only 0.2 mm, which is characteristic of commercial 30 vol.% composites.

SFF tests were conducted at room temperature (RT) at a strain rate of 10^{-4} s^{-1}, on a servo-hydraulic testing system. Strains were monitored by a 25.4 mm gage length extensometer attached to the gage length of the specimen. Two acoustic emission (AE) sensors, located at the two shoulders of the specimen, were utilized to detect fiber breaks. The signals were processed using a LOCAN unit (from Physical Acoustic Corporation), and utilized a position detection methodology based on time-of-flight information from the two sensors. The sensors were calibrated using pencil breaks, and location calibration procedures indicated that event locations could be pinpointed to within 1–2 mm, although in some cases the error was larger (~3 mm).

The error notwithstanding, the position information was used solely for the purpose of eliminating signals that could occur in the grips, and for obtaining an *in situ* estimate of fiber fracture localization behavior.

The SFF tests were continued to approximately 4.5% strain, since fiber fractures appeared to tail off at this value, indicative of attainment of fiber break saturation. Although higher strains (> 10%) can be imposed on the matrix, there is the strong possibility of excessive fiber damage caused by the titanium matrix and the brittle reaction zone at the coating–matrix interface. Consequently, additional fiber failures would likely belong to a different strength population, and unusually skew analyses of the SFF data. This problem does not exist for the much softer polymer matrix in PMCs. The 15-fiber specimens were unloaded after about 1.5% strain, a level that was considered sufficient to assess load sharing behavior for the three different interfaces. The 40-fiber specimens were loaded to failure (approximately 1.2% strain).

After mechanical testing, the fiber break locations were determined using an ultrasonic shear-wave back reflection (SBR) technique. The details of this technique are available elsewhere[15–17], and it relies on the concept of using shear elastic waves to excite the interface parallel to the fibers, and then analysing the intensity of the reflected shear waves using micromechanical modeling. At break locations, the intensity of the reflected wave undergoes drastic changes due to destructive interference between waves reflected from the intact and from the broken (and debonded) portions of the fiber, thereby allowing detection of the fiber break. Additionally, the axial distance over which the reflected wave intensity is different from the unbroken portion of the fiber provides a measure of the debond length, since the reflected wave intensity is highly sensitive to local stiffness variation; the latter, in turn, should represent altered bonding (i.e. debonded) conditions at the interface. Fragment lengths were determined from such ultrasonic measurements. A few specimens were etched to reveal the fiber fracture locations, and they correlated extremely well with the ultrasonic inspection. furthermore, excellent agreement was obtained between the number of fiber breaks measured by the AE technique, and those by the ultrasonic and etching technique; typically within two to three fiber breaks. The fiber fracture locations extracted from the AE data also correlated (within 1–2 mm) with locations obtained by the ultrasonic SBR technique. These consistencies provided significant confidence in the data from the SFF and MFF tests.

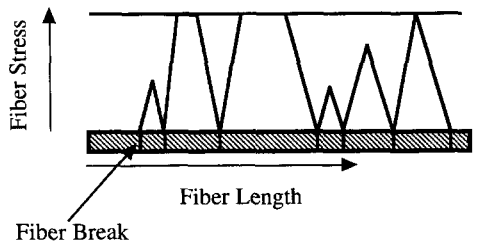

Figure 3 Sketch illustrating the random locations of fiber fractures, and the associated build-up of axial stresses on either side of the break. This type of random configuration is used in Curtin's analysis, as well as in the simulations performed here

DATA ANALYSES

To our knowledge, this is probably the first application of Curtin's model[14] for analysis of the SFF test. The detailed mathematical description is available in Curtin's paper, but the procedure is summarized here for easy reference and to illustrate how the model was used to analyze the experimental data.

In the model, fiber fractures are allowed to occur randomly (see sketch in *Figure 3*), but associated with a fiber break there is an exclusion zone where no fiber fracture can occur on further loading. The fiber break evolution is given by the following set of equations:

$$\frac{dL}{d\delta} = -\frac{q(\eta)}{\delta} \tag{2}$$

$$\frac{dN}{d\delta} = -\frac{L}{\delta^2}q(\eta) + \frac{2L\tau m}{rL_0\sigma_0}\cdot\left(\frac{2\tau\delta}{r\sigma_0}\right)^{(m-1)}\cdot\phi(\eta) \tag{3}$$

where $q(\eta) = 2\int_0^{\eta}\psi(\eta')\,d\eta'$, and $\phi(\eta) = 1/(\psi'(\eta))$, $\eta = (N/L).\delta$ and $\delta = (r\sigma)/(2\tau)$ is the shear lag distance. ψ is related to η through the implicit equation

$$\eta = \int_0^{\psi}\exp\left\{-2\int_0^{t}\frac{1-e^{-s}}{s}\,ds\right\}dt \tag{4}$$

Here, N is the number of breaks at any point in time, and L is the length of fiber available for further fracturing at higher stresses; note that L monotonically decreases with loading, while N increases with loading. The initial conditions are the initial length, $L = L_t$ of the fiber, and $N = 0$. Eqns (2) and (3) are integrated with respect to δ, which represents an increment of the stress level, through the shear lag equation stated above. The parameters r, σ_0 and m are the radius, *in situ* Weibull strength and Weibull modulus of the fibers, respectively, with the Weibull parameters determined at a gage length, L_0. Specifically, the fiber failure probability (P_f) at a gage length, L, and stress, σ, is given by

$$P_f = 1 - \exp\left\{-\frac{L}{L_0}\cdot\left(\frac{\sigma}{\sigma_0}\right)^m\right\} \tag{5}$$

In this work, L_0 was selected as 25.4 mm, although any other length scale can be chosen. The choice of L_0 was based on the fact that the strengths of fibers (both as-received, and after etching away from the matrix) were independently determined by testing fibers at 25.4 mm gage length. Integration was performed up to saturation, at which point η tended to the limit, $\eta^* = 0.7476$.

In the computational procedure, the explicit functions $\psi(\eta)$, $q(\eta)$ and $\phi(\eta)$, were determined initially. For a selected set of material parameters, i.e. (σ_0, m and τ), the above equations were integrated to obtain a complete record of the stresses at which fibers breaks occurred, and the fragment length distribution. The analysis shows that when the breaks are ranked (starting with $i = 1$) in an ascending order of stresses, and the probability (P) of failure calculated using the equation

$$P = i/(N_T + 1) \tag{6}$$

where i is the rank for the break, and N_T is the total number of breaks, then a plot of $\ln\ln(1/(1\text{-}P))$ *versus* $\ln(\sigma)$ follows very nearly a straight line with a slope of m (within 95% of the m selected for the calculations). This behavior, therefore, indicates that if the experimental data also is ranked and the probability determined from eqn (6), then a double logarithmic plot would provide the *in situ* Weibull modulus of the fibers. Accordingly, this procedure was selected for analysing the experimental data. Note that the Weibull strength or the friction stress cannot be determined from such a plot. Additional data is required for further analysis, and the fragment length distribution obtained by the SBR technique (or etching) fulfills that link.

In short, two plots are obtained from the experimental data: (i) the stress at which fiber breaks occur; and (ii) the cumulative fiber fragments as a function of fragment length. These data sets are then compared with parametric curves obtained from the computational results from eqns (2)–(4). The parameters for the material are based on that set that best fit the experimental data. Note that there is very little ambiguity in selecting m. The stress plot is also dependent on the Weibull strength. Finally, the cumulative fiber fragments are very sensitive to the friction stress. Indeed, we have found that there is a rather unique combination of parameters that can fit both sets of experimental data, thus defining the parameters for the particular composite. It is also useful to note that when the breaks are arranged in an ascending order (N) of breaking stress (σ), then a plot of $\ln(N)$ *versus* the $\ln(\sigma)$ also shows an almost linear behavior with a slope close to m (within 10%). Thus, such a plot can also be used to estimate m for the material. The advantage of this plot is that the fragmentation test does not have to be taken to saturation to determine the Weibull modulus. Additionally, the plot is useful when testing multiple fiber specimens for assessing load sharing behavior, since such specimens cannot be loaded to fiber-break saturation. This is because fiber fractures in MFF specimens become localized in a small section of the gage length, and composite failure occurs if the local volume fraction is of the order of 10% and higher.

We have also performed Monte Carlo simulation using a chain-of-links model with friction, to evaluate how Curtin's model compares with such a simulation. The simulations were carried out by dividing the fiber length into small bins (much less than the fiber radius), and breaking

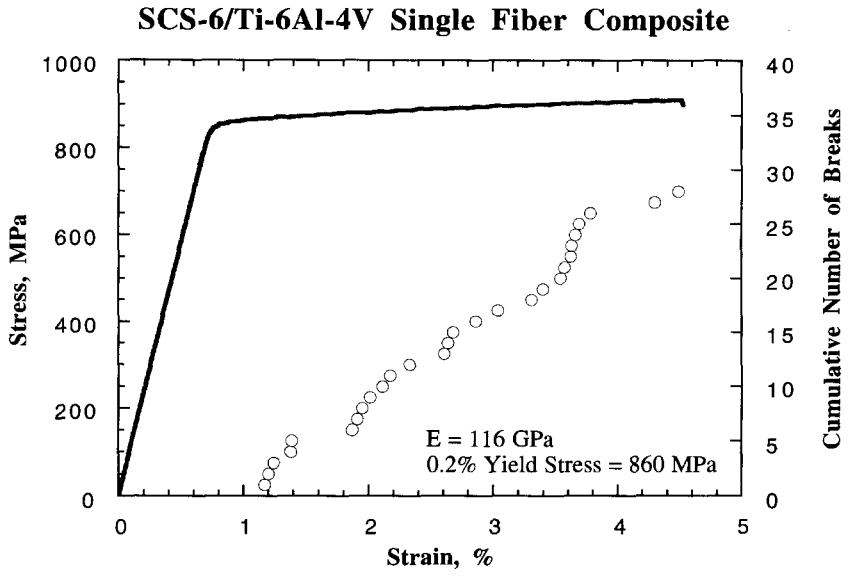

Figure 4 Stress–strain curve for the single-fiber SCS-6/Ti-6Al-4V specimen. Also illustrated are the strains at which successive breaks occurred

bins at different stresses based on the probability of fracture for the length of fiber available for breakage. The exclusion distance, where fiber fractures is prevented because the fiber stress cannot rise high enough, was based on the shear lag analysis with a constant frictional sliding stress. There was excellent correlation between the results from such simulation runs and Curtin's model, thus providing confidence in the data analysis that has been performed here.

RESULTS

Mechanical data

Figure 4 shows the stress–strain curve for a single-fiber SCS-6/Ti-6Al-4V specimen, and it indicates a fairly high yield strength of 860 MPa and a low work hardening response. The fiber-free matrix data was identical to this plot, consistent with the nearly zero volume fraction of fibers in the single-fiber specimen. The strains at which fiber breaks occurred are also indicated by symbols in *Figure 4*, where the fiber breaks were interpreted from AE signals that registered greater than 90 dB amplitude. The plot shows that the sample experienced 28 fiber breaks, in excellent agreement with 29 breaks determined by ultrasonic inspection.

Figure 5 illustrates the position detection capability of the AE signals for another specimen, where the distance of a break from one end of the gage length is plotted *versus* the ascending number (N) of the break event. The plot not only shows that the fiber fractures were generally contained within the gage length, but also it indicates where those signals came from during the duration of the test. While the fractures were distributed over the entire gage length, *Figure 5* shows that there were instances where succeeding fractures occurred close together, within 2 mm of each other. Other specimens revealed similar behavior, but with varying degrees of randomness. The local successive fracture events, spaced sufficiently long in time to discount any dynamically linked events, suggest possible fiber damage along the length of the fiber close to a fiber break, possibly through damage of the coating and the reaction zone. However, the degree of randomness between specimens prevent any definitive conclusion to be made at this stage. The data in *Figure 5* can be used to obtain a length distribution plot, and this compared reasonably well with the fragment length distribution obtained by etching away the matrix. Thus, the AE signals can in principle be used not only to detect a fiber break, but also to estimate where those signals originated in the specimen, in essence performing the role of *in situ* observation of fiber breaks.

*Figure 6*a and b illustrates inverted gray-scale images of the fiber obtained by the ultrasonic SBR technique for representative SCS-6/Ti-6Al-4V and Trimarc/Ti-6Al-4V samples, respectively. Fiber break locations are indicated by short white vertical lines in *Figure 6*(a), and illustrate a rather inhomogeneous distribution of fragment lengths for the SCS-6 fiber. For the Trimarc fibers [*Figure 6*(b)], the breaks (dark region between two adjacent white areas) have a clearer definition and the fragment length distribution is more uniform. The zones of altered intensity on either side of a break may signify interface failure and coating damage since those regions are anticipated to cause some stress-wave reversals, but additional analysis and observations are necessary to establish such a correlation. In a few samples, the matrix was etched away to reveal the fiber fracture locations, and the break locations and fragment lengths exhibited excellent correlation with the SBR data. It will be shown later that the fiber break did not consist of a single fracture event, but rather an aggregate of breaks that occupied a fiber length of up to one fiber radius. The center of the fractured zone was considered the center of the break,

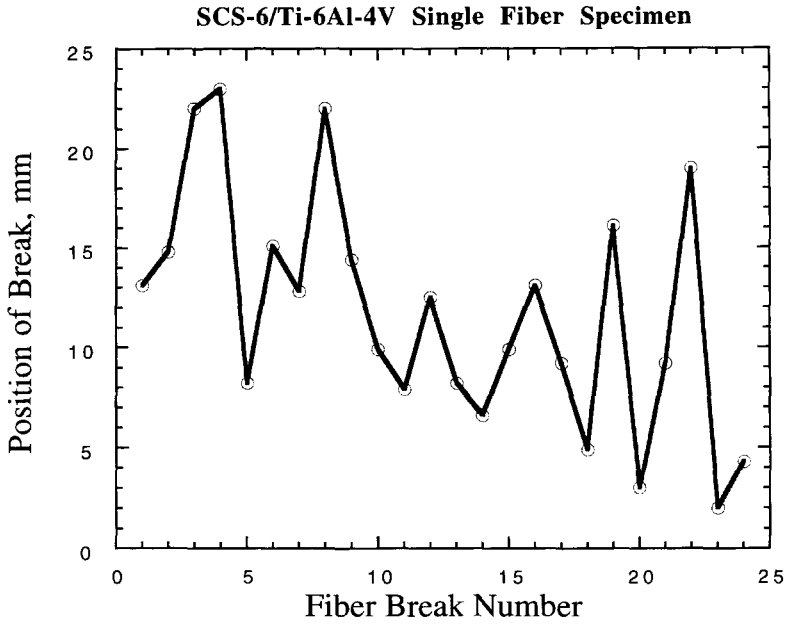

Figure 5 The position of a break detected by the AE transducers as a function of the cumulative number of the break in the SSF test. Note that there are a number of occasions where two successive breaks appear to originate in close proximity (within 1–2 mm), and that all the breaks are well contained within the 25.4 mm gage length of the sample

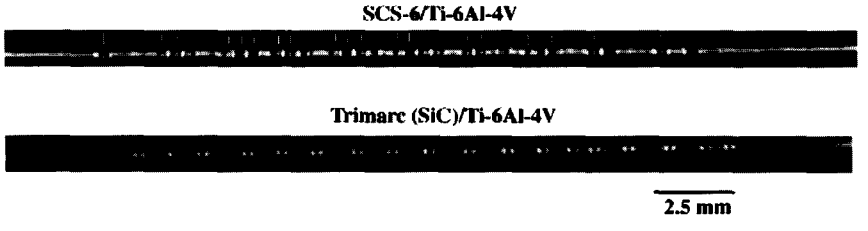

Figure 6 Shear wave back reflection (SBR) images of the single fiber fragmentation specimens: (a) SCS-6/Ti-6Al-4V, and (b) Trimarc SiC/Ti-6Al-4V. The fiber break locations in (a) are illustrated by the short white lines

and those positions were used to determine the fragment lengths.

*Figure 7*a is a Weibull stress plot obtained by the procedure outlined earlier. The fiber stresses at each break were obtained by the simple equation:

$$\sigma = (E_f.\varepsilon) - \sigma_{res} \quad (7)$$

where E_f is the fiber modulus, ε is the strain measured by the extensometer, and σ_{res} is the magnitude of the residual axial compressive stress in the fiber. The above equation is based on an iso-strain assumption, which may be violated at high strains as will be discussed later. A more sophisticated concentric cylinder model can be used in place of eqn (7), but it does not produce any significant changes in the final results. E_f for the SCS-6 fiber was experimentally obtained as 370 GPa and is consistent with other reported data (a range of 325–414 GPa) for SiC fibers. The residual stress was taken as 900 MPa, which was measured by cutting 25.4 mm segments of specimens, and etching away the matrix to obtain the change in length of the fibers. The residual stress is well below that based on a zero-stress condition at the processing temperature of 950°C, and is believed to be due to tensile loading of the single fiber by the matrix during the consolidation process.

In *Figure 7a*, the experimental data for three SCS-6/Ti-6Al-4V specimens are indicated by separate symbols. Also shown in the plot by the thick solid line is the theoretical curve based on Curtin's model, and using the parameters shown in the plot. *Figure 7b* is the corresponding fragment distribution plot, where the cumulative number of breaks is plotted *versus* the fragment length (x) normalized with respect to the average length (x_{avg}). Here, $x_{avg} = L_T/N_T$, where L_T is the gage length of the sample, and N_T is the total number of breaks. The normalization was performed to allow easier comparison between the fragment distribution data from different samples, since there were some variations in the total number of breaks (N_T ranged between 25 and 31 for the SCS-6/Ti-6Al-4V samples). The thick solid line in *Figure 7b* once again represents the results from Curtin's analysis, using the same parameters as those used in *Figure 7a*. Also shown by the thicker dashed line in *Figure 7b* is the result of our Monte Carlo simulation, performed with the same set of parameters. Its excellent agreement with Curtin's

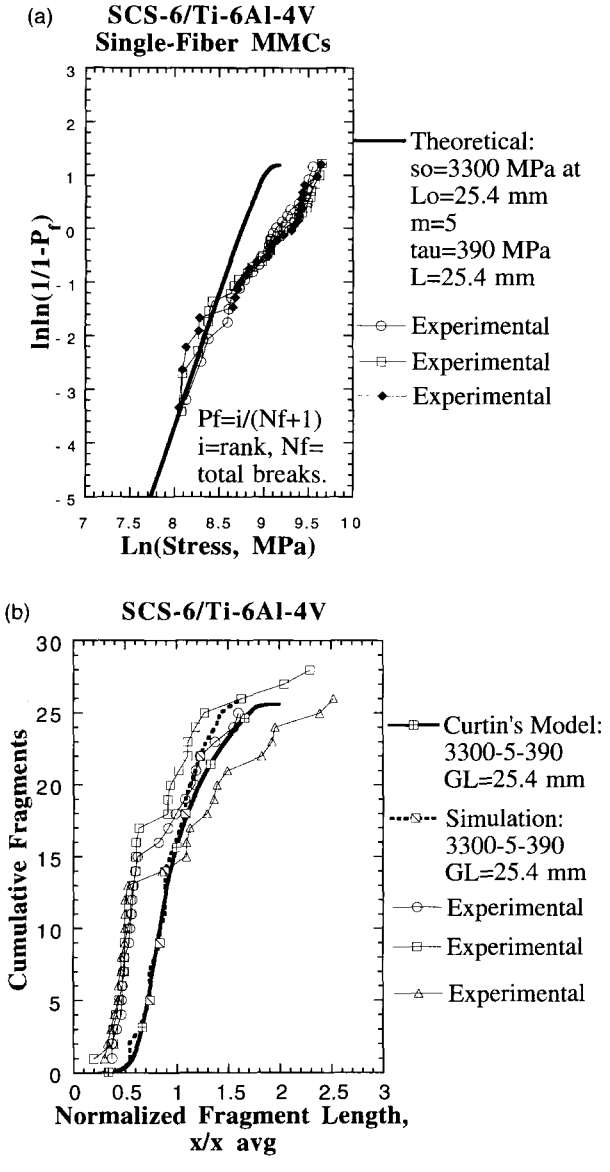

Figure 7 (a) Stress plot for the SCS-6/Ti-6Al-4V SFF specimens. The experimental data from three samples are indicated by the symbols, and the thick solid line is the result from Curtin's model with $m = 5$, $\sigma_0 = 3300$ MPa at $L_0 = 25.4$ mm, and $\tau = 390$ MPa. (b) Fragment length distribution plot for the same specimens. The thick continuous line is from Curtin's analysis, and the dashed thick line is from the simulations, using the same set of material parameters as in (a)

model may be noted. A similar correlation was observed on a stress plot, but was not included in *Figure 7a* for retaining clarity of that figure. The combination of the two figures (*Figure 7a* and *b*) represent the complete characterization of the SCS-6/Ti-6Al-4V SFF samples.

There are two important comments about *Figure 7a* and *b*. First the parameters, i.e. $\sigma_0 = 3300$ MPa, $m = 5$, and $\tau = 390$ MPa, were obtained by a parametric selection process, but aided by reasonably good initial estimates, based on the discussion that follows. As indicated earlier, the selection of m is straightforward, since it represents the slope of the stress plot (*Figure 7a*). The choice of σ_0 also follows primarily from the stress plot, but the total number of fiber breaks have also to be taken into account. Specifically, the expected (on the average) number of breaks in a fiber of gage length L that is stressed to a stress, σ, is given by:

$$N_{exp} = (L/L_0)(\sigma/\sigma_0)^m \tag{8}$$

By identifying N_{exp} with the total number of breaks (N_T) in a specimen, the stress (σ') corresponding to $\ln\ln\{1/(1 - P_f)\} = 0$ is simply

$$\sigma' = (L_0 N_T/L)^{1/m}.\sigma_0 \tag{9}$$

By reading off σ' (corresponding to $\ln\ln\{1/(1 - P_f)\} = 0$) from the Weibull stress plot, an initial estimate of σ_0 is obtained. Then, the approximate value of τ is estimated from eqn (1), by substituting σ' for σ in that equation, and identifying δ with $L_c/1.337$, where L_c is the average fragment length, equal to L/N_T. The factor 1.337 derives from the fact that fiber fragments, at break saturation, in a material with infinite Weibull modulus would still have lengths varying randomly between δ and 2δ, with a mean of -1.337δ[18,11–14], rather than 2δ as implicitly assumed in Kelly and Tyson's formulation[10]. These initial estimates of parameters are used in the exact analysis [eqns (2)–(4)] to obtain the distribution plots, and the parameters are then modified to best fit the experimental data.

The second point about *Figure 7a* is the apparent transition of the experimental data from a line with an initial higher slope to one with a subsequent lower slope. We believe that the fiber stress estimate at higher strains, using eqn (7), is inaccurate because iso-strain conditions may be violated: note that fiber failure strains are typically 1.0% for 25.4 long fibers, and the deviation in *Figure 7a* occurs at approximately 1.6% strain. The reason for the loss of isostrain conditions is the intense plastic deformation (interpreted from macroscopic slip bands) of the matrix at the fiber break locations, and severe fragmentation of the fiber at the breaks which likely aided in fiber-end separation. These evidences will be presented later. Consequently, only the initial part of the data in *Figure 7a* was used to estimate the *in situ* Weibull parameters.

Figure 8 shows the Weibull plot for SCS-6 fibers that were etched out of untested multiple fiber specimens. The fibers had a gage length of $L_0 = 25.4$ mm. The Weibull parameters obtained from the plot are $\sigma_0 = 4483$ MPa and $m = 13.6$, which are significantly different from the *in situ* parameters obtained by the single-fiber fragmentation tests. In *Figure 8*, the least-squares fit was performed by eliminating the three lowest strengths in the population. The reason is because previous work[19,20] with SCS-6 fibers has shown that the low-strength fibers, which exhibit considerable departure from the average in the Weibull plot, belong to a separate fiber population. That population consists of surface initiated failures (damage related), compared with internally initiated failures in the bulk of the fibers. In fact, previous findings[19,20] suggest that if only the data from fibers with surface initiated failures are considered, then the Weibull parameters are in the range $\sigma_0 = 2100$–2800 MPa, and $m = 4$–6. It is interesting to note that our current results from the SFF tests are in better agreement with these Weibull parameters (particularly m),

than the Weibull parameters represented by the line in *Figure 8*. While damage to the fibers *in situ* during SFF testing is a distinct possibility, it is difficult to justify comparison of the SFF results with the Weibull parameters of extracted fibers that only have surface initiated failures. Rather, these results in totality suggest that perhaps a more complex analysis with dual strength population may be worth considering, where the lower strength fractures actually occur at higher stresses (due to smaller available lengths), but which stresses are nevertheless lower (due to damage) than those expected from the original strength population for that fiber length. The Weibull parameters of the as-received fibers were $\sigma_0 = 4668$ and $m = 12.7$, which are similar to the etched fibers, indicating that the composite consolidation process *per se* did not have any significant damaging effect on the strength of the fibers.

In addition to the fiber strength tests, push-out tests were also performed on 0.6 mm thick samples. The load–displacement plots for the SCS-6/Ti-6Al-4V system showed an initial linear behavior, followed by a sharp load drop to about 85% of the previous maximum load (P_d), then a rapid increase in load which finally exceeded P_d after 3–4 μm of sliding displacement. Previous research on

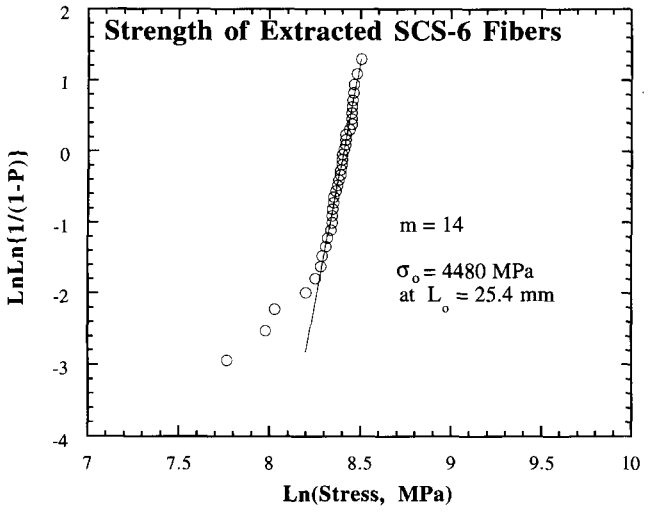

Figure 8 Weibull plot for SCS-6 fibers extracted from the composites using a Kroll's reagent

push-out testing[7–9,21] has shown that the load drop is associated with instability of the interface crack, which initiates at the face away from the indenter (the bottom face), rapidly traverses the thickness of the specimen, and completes that traverse by the time the minimum load (P_l) associated with the load drop is attained. The subsequent load increase is believed to be due to damage of the interface, caused by a combination of fiber surface roughness and the high clamping stress (approximately 300 MPa) at room temperature. Usually P_d is divided by $2\pi rt$, where t is the specimen thickness, to obtain an average shear debond stress (τ_d). The average shear stress ($P_l/2\pi rt$) associated with the minimum load is the frictional sliding stress, τ_f, since the entire fiber is sliding at this point. On the other hand, the load increase observed with the SCS-6/Ti-6Al-4V composite immediately after the load drop suggests that the frictional sliding stress is actually a function of the fiber displacement. Since that displacement is not known under fragmentation conditions, the frictional sliding stress for SCS-6 and SCS-0 fibers under push-out conditions is identified with the shear debond stress (τ_d), and that value is compared with the average shear stress, τ, obtained by fragmentation testing. This method of defining the frictional stress from the push-out test is consistent with what is often loosely used in the push-out/pull-out literature, although it should be noted that the shear debond stress, τ_d, is strictly a function of the frictional stress, τ_f, and the fracture toughness of the interface[9,22]. In the case of Trimarc fibers, the load remained constant after the debond event, so that the frictional stress under push-out conditions was identified appropriately with the constant sliding load, rather than the maximum load, P_d. The push-out tests indicated a τ_d of 160–190 MPa for the SCS-6 fibers in the Ti-6Al-4V matrix. These numbers are slightly higher than push-out data reported in the literature[23], but are well below that obtained from the fragmentation test. In the case of Trimarc fibers, the frictional stress from push-out tests was only 30 MPa, indicating that these carbon coatings are much weaker (or have lower frictional coefficient) than the coatings in SCS-6 fibers. The details of the coatings are provided later in this paper.

The Weibull parameters and the frictional stresses are listed in *Table 1*, and includes data from the SFF tests, the fiber strength tests, the push-out tests, and reported data[24,25]

Table 1 Interface and fiber strength data for the SiC/Ti-6Al-4V systems

Fiber	Extracted fiber Weibull strength, σ_0, (L_0 = 25.4 mm) MPa[a]	Weibull modulus, m, of extracted fibers	Push-out shear stress, τ (MPa)	Normal (tensile) intreface strength	Fragmentation strength, σ_0 (MPa) (L_0 = 25.4 mm)	Fragmentation Weibull modulus, m	Fragmentation average shear stress, τ (MPa)
SCS-6[b]	4480	14	160–190[c]	100–120	3300	5	390
Trimarc[d]	3400	20	30[e]	~0–20	3050	9	190
SCS-0[f]	1500	6	290–320[c]	~380	1300	6	500

[a]The corresponding average strength of fibers is $\sigma_{avg} = \sigma_0.\Gamma\{(m + 1)/m\}$, where Γ is the gamma function, and m is the Weibull modulus.
[b]Has graded turbostatic-C plus fine-particulate-SiC coating (~3.5 μm thick). Made by Textron.
[c]Debond stress, τ_d, corresponding to the maximum load before the load drop. After the load drop, the load increases rapidly in the case of the SCS-6 fiber, and reaches τ_d within 3–4 μm of sliding displacement.
[d]Has a hard–soft–hard turbostatic carbon coating (~3 μm thick). Made by Amercom.
[e]Sliding stress in the constant load region following debonding. The debond stress, τ_d, is also very similar to the frictional sliding stress for this fiber.
[f]Has no outer coating on the bare SiC fiber. Made by Textron.

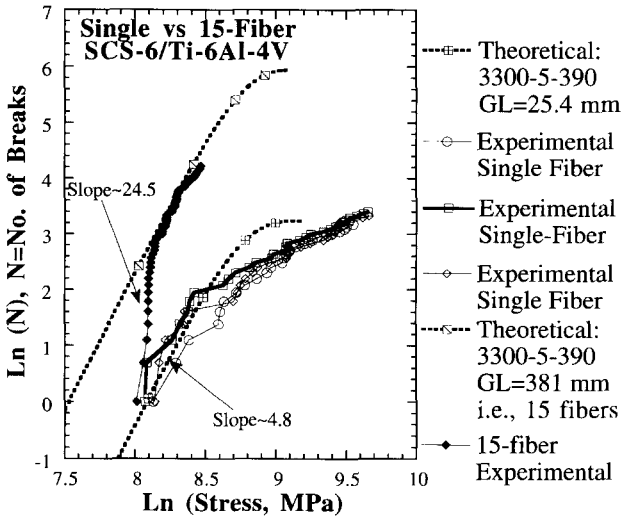

Figure 9 Stress plot for the 15-fiber SCS-6/Ti-6Al-4V sample compared with the SSF data. The ordinate here is the cumulative number of breaks. The experimental data are illustrated by symbols, the lower thick dashed line corresponds to the results from Curtin's model for a gage length of 25.4 mm, and the upper thick dashed line corresponds to the analysis with 381 mm length of fiber (corresponding to the 15-fiber specimen)

on the tensile (normal) strength of the interfaces. There are significant differences between the data sets, and they will be discussed in the next section.

Figure 9 is a stress plot for a 15-fiber SCS-6/Ti-6Al-4V specimen, where $\ln(N)$ is plotted *versus* the logarithm of the breaking stress, $\ln(\sigma)$. As indicated earlier, this method of plotting is necessary because damage localization in such a specimen does not allow fiber fracture saturation of each individual fiber. *Figure 9* includes data from the SFF tests, as well as the theoretical curve for a gage length of 25.4 mm, using parameters that were determined earlier, i.e. $\sigma_0 = 3300$ MPa, $m = 5$, and $\tau = 390$ MPa; the designation in the plot is 3300-5-390. Also included in *Figure 9* is the theoretical single-fiber curve for the same set of parameters, but for a total fiber length of 381 mm (15 fibers $\times$ 25.4 mm $=$ 381 mm). The basis for this latter curve is that the fiber break accumulation in a single-fiber specimen with a total gage length of 381 mm should be identical with that for the 15-fiber specimen with a gage length of 25.4 mm, when there is no interaction between those 15 fibers. On the other hand, any interaction between neighboring fibers would manifest in the form of a lack of agreement between the experimental data and the base 381 mm single-fiber theoretical curve.

Figure 9 shows that although the 15-fiber specimen approached the theoretical curve at higher stresses, the experimental data significantly deviated from the 15-fiber theoretical curve at lower values of stresses. During the initial stage, when fiber strain is well represented by the measured strain, such that eqn (7) is valid, the slope for the experimental data is higher than the theoretical slope by about a factor of 5. Since, as discussed earlier, the slope of the curve represents the Weibull modulus, the 15-fiber data suggests a higher apparent Weibull modulus for the fibers. Since there is no reason why the *in situ* fiber statistics

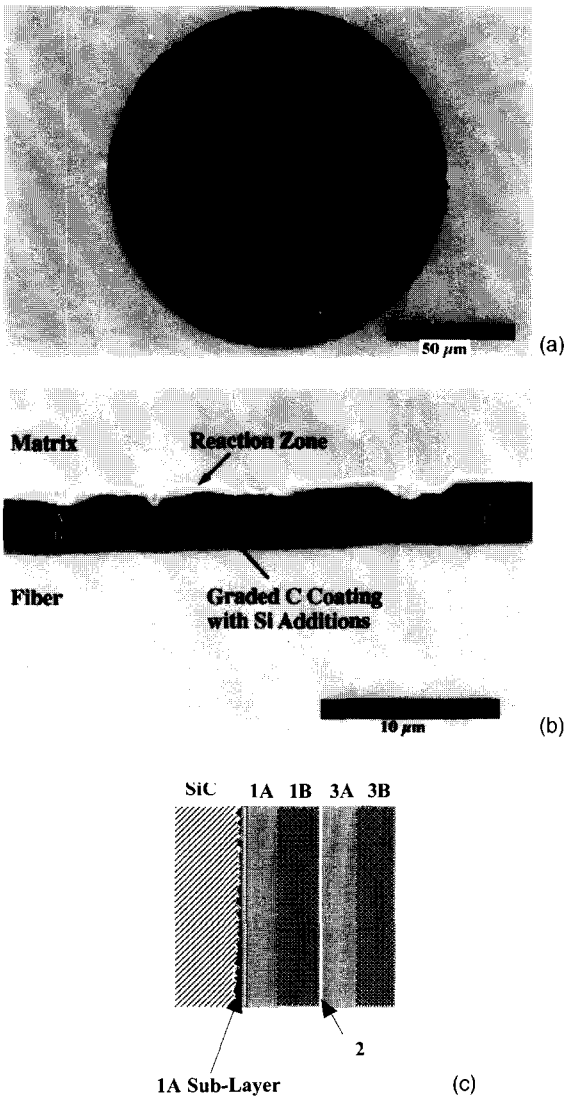

Figure 10 (a) Cross-section of the as-processed SCS-6/Ti-6Al-4V composite. (b) Longitudinal section of the as-processed composite in the region of the coating. (c) Sketch, illustrating the different coatings of the SCS-6 fiber, based on the findings of Ning and Pirouz[26]. The trace of the line AA in (b) corresponds approximately to region 2

should differ from the SFF samples, the higher apparent Weibull modulus may be interpreted as being due to a stress-concentration effect between neighboring fibers. This is because the occurrence of a break under stress-concentration conditions would quickly load up fibers in adjacent locations, thus setting up a succession of breaks with very little increase required in the applied stress–strain. In essence, this would manifest as a higher Weibull modulus. Evidence of this mechanism will be presented in the next section. In *Figure 9*, the lower slope at higher stresses is once again a result of the fiber stress not being represented by eqn (7), since isostrain conditions are violated due to localized plasticity, as will be shown in the next section.

Microscopy

Figure 10a illustrates the cross-section of the SCS-6 fiber in the Ti-6Al-4V matrix. The dark region corresponds to

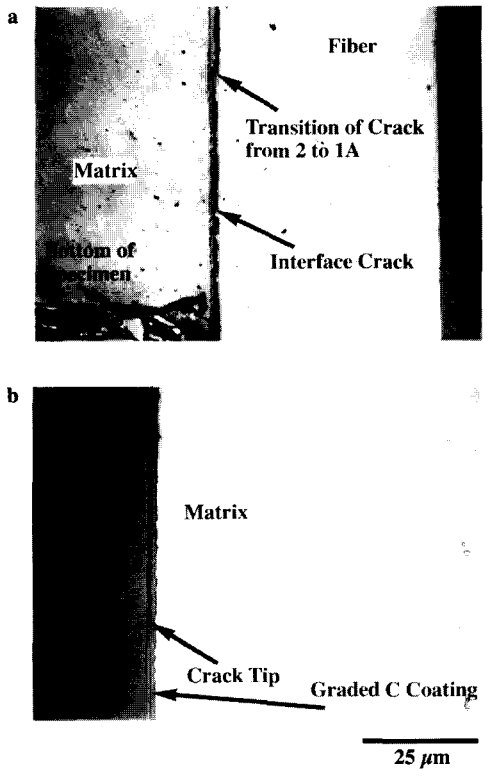

Figure 11 Optical micrographs of a longitudinal section, illustrating interface failure locations in a SCS-6/Ti-15-3 composite. (a) Micrograph illustrates that the interface crack tends to switch locations, although it generally is confined to region 1A of *Figure 10c*. (b) Close-up of an interface crack that has terminated inside the specimen, revealing that it is confined to region 1A

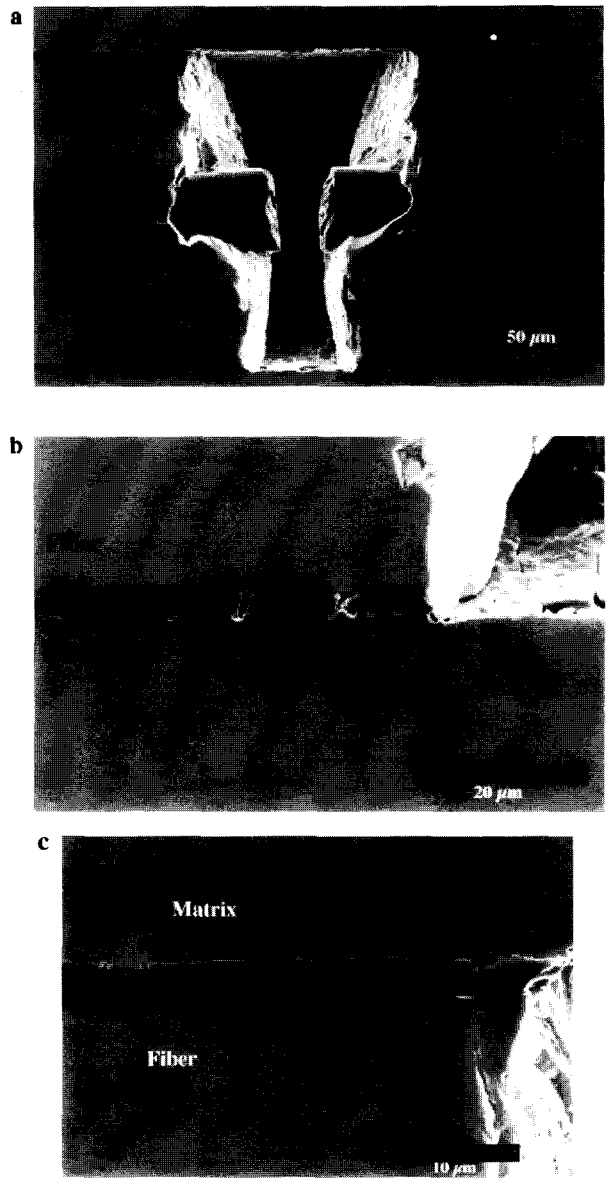

Figure 12 (a) A fiber break location in a SCS-6/Ti-6Al-4V composite. It shows that the break actually consists of severe fragmentation of the fiber over a length less than one fiber radius, and that there is interphase damage on either side of the break. (b) A higher magnification micrograph at the location of the break; the fiber is at the top. (c) Another region similar to (b), illustrating damage in the reaction zone and the coating, but a lack of any strong evidence of a shear crack in the coating originating from the break

the carbon coating on the fiber, and the flowery feature is a result of uneven reaction of the coating with the matrix; the reaction being greater in the beta phase of the alpha–beta Ti-6Al-4V matrix. *Figure 10b* is a high magnification micrograph of the turbostatic coating region of the as-received material, on a longitudinal section. The coating essentially consists of turbostatic carbon with the *c*-axis generally oriented along the radial direction of the fiber, and containing different amounts of SiC particles. In order to understand where coating failures can occur, and to assess the possibility of fiber damage by a crack in the coating, we provide the sketch of the SCS-6 coating (*Figure 10c*) based on a previous work[26]. Notable is the fact that the SiC has sharp saw-tooth surfaces, arising from the lenticular morphology of the SiC grains, although the peak-to-peak height of the saw-tooth appears to be limited to the range 10–20 nm. The saw tooth is smoothed by a 0.15 μm carbonaceous layer containing fine SiC particles, and this is followed by the regions 1A–3B. Regions 1A and 3A are similar, containing coarse (10–50 nm size) SiC particles, and regions 1B and 3B are similar, containing a significantly higher volume fraction of much finer SiC particles. Region 2 is only 50 nm thick, is essentially devoid of SiC particles, and interface cracks under push-out testing in a silicon nitride matrix generally occur in this layer[27]. Returning to *Figure 10b*, the trace of an interface along line AA corresponds to the layer 2, and the trace along BB corresponds to the transition between region 1A and 1B. These transitions can also be seen using optical microscopes, presumably due to different contrast of the layers as well as surface relief due to different hardnesses. In addition, they are consistent with the scanning and transmission microscopy work in Ref.[28] for the SCS-6/Ti-15-3 TMC. It is also important to note that region 3B is almost completely consumed by the Ti-6Al-4V matrix.

Under push-out conditions in a TMC, interface failure does not appear to be restricted to layer 2, as is generally observed in ceramic matrices, such as silicon nitride. Rather, as shown in *Figure 11a* and *b* for a SCS-6/Ti 15-3 TMC (B.S. Majumdar, unpublished research), the interface crack propagates either in layers 2 and 1A, with transitions often observed between them. While it is generally very

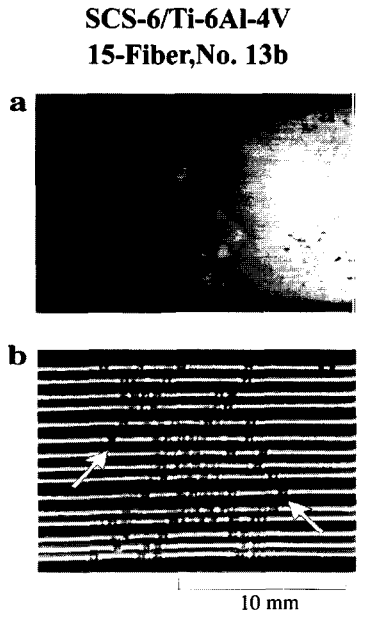

Figure 13 (a) Macroscopic slip bands on the surface of the 15-fiber SCS-6/Ti-6Al-4V specimen, whose data was shown in *Figure 9*. (b) SBR image of the same specimen, showing a one-to-one correspondence between the intersection of slip bands and the fiber break locations

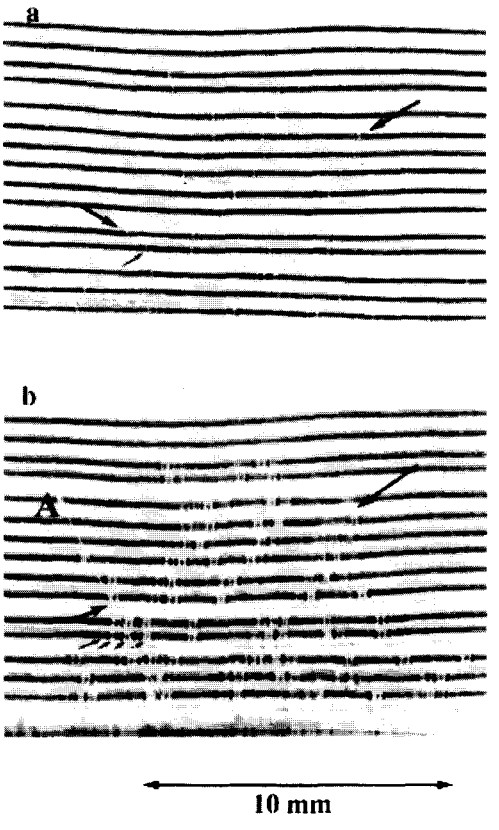

Figure 14 SBR images of a 15-fiber SCS-6/Ti-6Al-4V specimen, at two different levels of strains. The number of fiber breaks have increased in going to a higher strain value in (b). The path of progression of the fiber breaks (such as trace A) agree with the direction of propagation of slip bands (not shown here)

difficult to see shear cracks in the carbon coating, our overall observation has been that the interface crack under push-out conditions is more common in region 1A, which is very close to the saw-tooth (albeit nanometer scale) fiber surface. An interface crack parallel to the fiber axis in layer 1B is not observed. Rather, this layer is rather prone to transverse cracking by a crack perpendicular to the fiber axis, possibly because the *c*-axis of the turbostatic carbon blocks in this layer are not as well oriented along the radial direction, and thus do not present a weak interface where normal debonding can occur. Under transverse loads, interface cracks are observed in layers 2, 1A, and at the interface between the carbon coating and the reaction zone, with layer 2 being the more common site[24,29,30].

Figure 12a is a low magnification micrograph of a fiber break in the SCS-6/Ti-6Al-4V fragmentation sample. It illustrates that the fiber fracture does not occur on a single plane, but rather it involves multiple fractures and consumes a total length of up to one fiber radius. The crushing and severe fragmentation of the fiber at the break allows the matrix to cave in, likely increasing the local interface radial stress at the ends of the break. The shorter fragment lengths in *Figure 7b* are of the order of 0.4–0.6 mm. These lengths are larger than the crushing length (one fiber radius), so that those fragments do constitute distinct entities and were correctly included in the data analysis procedure.

Figure 12b and *c* are high magnification micrographs of the interface region at two different break locations. They provide little evidence, if any, of any interface shear crack having propagated from the break, as is assumed in shear lag models. However, the lack of evidence should be considered in the context that it is extremely difficult to locate shear cracks in these carbonaceous coatings. In contrast to the absence of a continuous shear crack, there are two types of damages that can be observed at the interface. One is the significant number of transverse reaction zone cracks (presumably formed because of the large strain in that region), some of which travel transversely through the coating and stop in layer 1A. Although some of these transverse cracks appear to kink at layer 2, they are not stopped, and propagate onto layer 1A. The other type of damage are the discontinuous shear cracks which tend to be localized in layer 1A. As indicated earlier, these cracks are very close to the fiber surface, and pose the threat of damaging the fiber, particularly if there is a large clamping stress which increases the frictional resistance. This is because a higher frictional stress essentially acts to raise the local interface toughness[9], thereby favoring crack kinking into the fiber in preference to continued propagation of the interface crack[31].

Figure 13a and *b* corresponds to the 15-fiber specimen whose data were plotted in *Figure 9*. *Figure 13*a is a macroscopic view of the specimen face, and shows a crisscross pattern of slip bands that are concentrated in a relatively small section of the gage length. *Figure 13b* illustrates the fiber break locations, as imaged by the SBR technique, and shows a one-to-one correspondence between the slip band intersections with the fiber and the fiber break locations. The intense but macroscopic slip bands are not observed in the unreinforced material, nor can they be seen

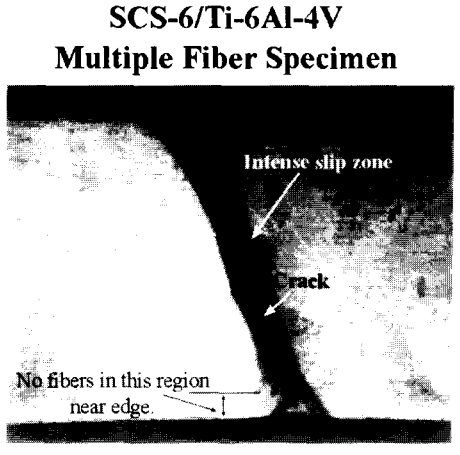

Figure 15 Face of a 40-fiber SCS-6/Ti-6Al-4V specimen ($v_f = 11.6\%$) pulled to failure at 1.2% strain. The zone of the intense slip band and the crack path is indicated. SBR imaging shows absence of any fiber break away from the intense slip zone

near the specimen edges in *Figure 13a* because the fibers are located a small distance away from the edges. Together, *Figure 13a* and *b* indicates that fiber fractures have occurred cooperatively, with localized matrix plasticity being responsible for the cumulative failure of fibers. This type of LLS behavior is consistent with the higher Weibull modulus for the 15-fiber specimen compared with the single fiber specimen (see *Figure 9*).

To further illustrate the progression of fiber failures and localized matrix plasticity, we present *Figure 14a* and *b* for a 15-fiber SCS-6/Ti-6Al-4V specimen, at two successive loading steps (the specimen was unloaded after each loading step). There was a small extent of fiber swimming in this specimen, as evidenced by some bowed fibers, and fiber fractures initiated from one edge (in the width direction) of the specimen and propagated towards the other edge. In addition, the SBR imaging conditions were slightly different for the two micrographs, but both clearly show the location of the fiber breaks (see arrows) at different levels of strain. There are two comments about *Figure 14*. First, similar to *Figure 13*, *Figure 14a* indicates that fiber breaks tend to be aligned along rays that are roughly 45–60° to the loading axis, although there are a few exceptions. These rays are precisely along directions where macroscopic slip bands can be seen on the specimen face, similar to *Figure 13b*. *Figure 14b* shows that new breaks form along those rays, suggesting that they form as the slip bands from the existing fiber breaks impinge on the adjacent fiber; see, for example, trace A in *Figure 14b*. The specimen face also shows slip band extension along the rays, confirming the role of localized plasticity in inducing local fiber failures. Second, the fibers are much more fragmented at the original break locations, and those additional breaks were also confirmed by matrix removal by etching. Thus, as the extent of plastic deformation in the each major slip band increases, so does the number of breaks for a fiber within that band, consistent with the results from the single-fiber fragmentation tests. Whereas a simple shear lag analysis, using friction stress data from push-out tests, would suggest that additional fragments of a fiber should not occur within a band, *Figure 14b* shows results to the contrary. This behavior is suggestive of a high friction stress, or possibly no debonding in the classical sense, as suggested by *Figure 12b* and *c*.

In order to see how these low volume fraction results translate to higher volume fractions, *Figure 15* is provided. This single-ply specimen had 40 fibers approximately 200 μm apart, that is characteristic of typical 30 vol.% multi-ply composites; the overall volume fraction was approximately 11.6% because of excess thickness and width of the specimens. The mechanical data showed the characteristic knee in the stress–strain curve[29,30], followed by composite failure at approximately 1.2% strain and a stress of 1160 MPa. Only about five AE events were registered before catastrophic failure, at which point the number of breaks was so large that they could not be recorded by the AE instrument. SBR imaging showed that the fibers were highly fragmented in the intense slip zone that traversed the specimen at approximately 60° to the loading axis. The orientation of this major slip band is consistent with the directions observed in the 15-fiber specimens, and suggest that here too there was a synergism between the slip bands and fiber fracture locations. No breaks were observed outside the highly strained zone, so that the fracture behavior suggests LLS for this system, although SCS-6 fibers are generally known to possess a weak interface and hence should foster global load sharing. It may be mentioned here that a similar failure morphology was observed for a 40-fiber Trimarc/Ti-6Al-4V sample, which has a much lower interface frictional stress (see *Table 1*), and for which the *in situ* Weibull strength under SFF conditions was quite close to that measured by testing individual extracted fibers. Thus, this mode of failure, aided by intense plasticity, is characteristic of the composites tested at room temperature, for interfaces that are generally considered as weak. What was also quite surprising is that a 40-fiber SCS-O/Ti-6Al-4V specimen showed a much more uniform damage state, in that the entire gage length was crisscrossed by a network of intersecting bands, rather than a concentrated plane of fiber fractures. This specimen exhibited a constant flow stress of 730 MPa, well below that of the unreinforced matrix, indicating that the load was being extensively carried by the plastically deforming zones.

DISCUSSION

An approach has been outlined here for extracting interface and fiber strength parameters from single fiber fragmentation specimens. As indicated earlier, the interface stress conditions in this geometry closely resemble the stress state following fiber fractures in a longitudinally loaded bulk composite. Therefore, this geometry is preferable to push-out/pull-out tests when considering interface design in the context of longitudinal strength of a composite.

Past approaches in SFF testing have generally relied on the well-known Kelly–Tyson equation that neglects the

statistics of fiber failure, so that there have been concerns that the equation does not provide adequate understanding of the fiber fragmentation process. Among other approaches that are available for analysing the fragmentation test, Curtin's analytical model[14] appears to capture the essentials elements of the fragmentation phenomenon, and consequently this model was used in this work. In addition, our simulation using the chain-of-links approach showed that Curtin's analytical formulation does indeed provide excellent description of a stochastic fiber fragmentation process. The experimental data were analyzed by taking two essentially independent data sets (i.e. the fiber breaking stress and the fragment length distribution), and determining three parameters, i.e. σ_0, m and τ, that provided best agreement with the data sets. The method by which good initial estimates of the parameters can be made has been described in this paper.

The combination of AE signals and SBR imaging provide a powerful method of analysing opaque samples, such as metal matrix composites The fiber fractures in SCS-6 and Trimarc fibers have characteristic AE amplitudes greater than 90 dB, and results show excellent agreement with SBR and metallographic results. Although not described here, uncoated SCS-0 fibers do not, however, show this amplitude, but rather have signatures at the 78–88 dB level. This is likely related to the lower strength of the fibers, and has the effect that there are larger errors in assessing when SCS-0 fibers fail in the SFF test.

The SBR technique proved to be excellent for detecting fiber break locations nondestructively. The images were not only useful for determining the parameters of the SFF test, but more importantly its real potential lay in analysing local *versus* global load sharing behavior in multiple fiber specimens. Excellent correlation was obtained between the slip bands intersections and the location of fiber breaks, and these were verified by etching away one side of the matrix and comparing micrographs with ultrasonic images. Additionally, the SBR method is essential for following the progression of fiber breaks through interrupted testing.

The SFF results with the SCS-6 fiber indicate that the Weibull and the average shear stress are significantly different from those determined by alternate techniques. Thus, the average shear stress under fragmentation conditions was 390 MPa compared with 160–190 MPa determined by the push-out test. One likely reason is the greater clamping of the fiber at the location of break. This has been discussed in past papers[32–35]. In particular, ref.[34] shows that the radial stress is singular, although it attenuates very rapidly along the length of the fiber. In ref.[35], analysis with a discontinuous fiber showed that the compressive radial interface stress in the immediate vicinity of the break was of the order of the axial stress in the matrix, which is the flow stress in the SFF samples. The significant fragmentation of the fiber at the location of a break, and subsequent collapse of the surrounding matrix may also contribute to additional clamping, although the mechanics need to be analyzed. Elastic–plastic calculations using the concentric cylinder model indicate that in the absence of a fiber break the clamping stress is not significantly different from the residually stressed state. Thus, the clamping that occurs must be very local in nature. If the average shear stress of 390 MPa in the SFF test is assumed to arise only from a Coulomb effect, and if a friction coefficient of 0.5 is assumed for the SCS-6 coating (based on RT push-out data and a RT radial residual stress of approximately 300 MPa), then we obtain a local radial stress of approximately 780 MPa. This is of the order of the flow stress of the matrix, which is consistent with the analysis in ref.[35]. However, a more rigorous analysis is necessary to confirm the level of radial stress at the interface in the vicinity of a fiber break.

Another difficult issue to rationalize is the difference between the Weibull parameters obtained from the SFF test, and the parameters determined by testing extracted fibers. The lower Weibull modulus and Weibull strength obtained from SFF tests for the SCS-6 fibers suggest that there may be damage sites in the fiber that are being activated under fragmentation conditions. Thus, both *Figure 6a* and *Figure 14b* show a bimodal distribution of break locations, in that there are a number of widely separated breaks and a number of closely separated breaks. This type of break distribution is also evident in *Figure 7b*. A possible scenario is that interface damage near an existing break can introduce an interface crack in region 1A (see *Figures 11* and *12b* and *c*) which is next to the fiber. If this crack experiences high frictional stresses, the local resistance to interface crack propagation may make conditions suitable for such a crack to kink into the fiber, aided by the saw-tooth profile of the SiC surface in the SCS-6 fiber. Additional experiments and observations are required to confirm fiber damage, some of which are currently under investigation. If indeed there is damage to the fibers, the analysis will have to be modified to take into account two possible flaw distributions, such as was done in Ref.[36]. In the case of Trimarc fibers, the break locations (*Figure 6b*) did not give any indication of a bimodal distribution of fragments. Additionally, the Weibull strength was close to that obtained by testing extracted fibers. Thus, this fiber appears to be less prone to damage, and may be a result of the fact that the coating consists solely of turbostatic 'soft–hard–soft' carbon without silicon additions, and also possibly due to a smoother SiC surface.

The multiple fiber tests at room temperature were very revealing. The mechanical data showed a five-fold Weibull modulus increase compared with the single-fiber specimens, suggestive of correlated fiber fractures. The AE data and SBR images showed that fiber failures were concentrated in a relatively small section of the gage length, and the location of the fiber failures correlated with intersection of macroscopic slip bands with the fibers; those slip bands do not occur in the fiber-free material. The results indicate that localized plasticity that ensues from a broken fiber plays a dominant role in precipitating failure in the adjacent fiber, and the mechanism is illustrated by the sketch in *Figure 16*. The unanticipated result was that the phenomenon was observed for the weak interfaces (Trimarc and SCS-6), since global load sharing is generally expected to occur when the interface shear strength is less than 10% of the fiber

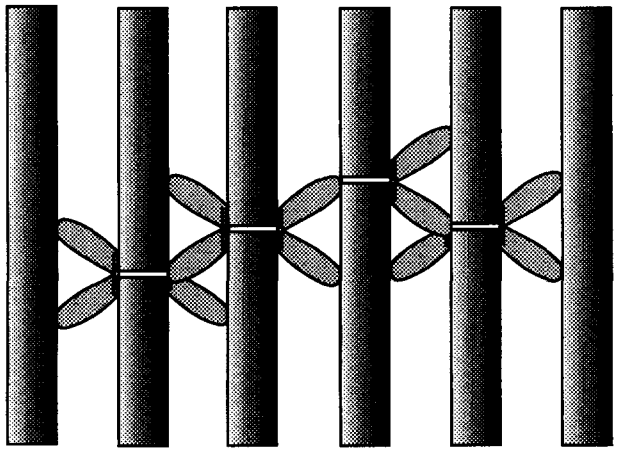

Figure 16 Sketch illustrating the mechanism of slip induced local load sharing in TMCs at room temperature

strength[37]. It is important to note, however, that the results are not inconsistent with ref.[37], since local load sharing is predicted to always occur for single ply specimens, independent of the friction stress. However, the mechanism of localized plasticity and its influence on adjacent fiber fractures are different and need to be modeled rigorously.

Although the work so far has concentrated on single-ply specimens, there are evidences which suggest that local load sharing dominates in other multi-ply SCS-6/Ti-alloy composites at room temperature. Thus, experimental strengths of multi-ply SCS-6/Ti-25Al-17Nb[38] and SCS-6/Ti-1100[39] were well below strengths predicted by Curtin's global load sharing model[40]. Matrix etching showed little, if any, evidence of fiber fracture in the gage section except in a very thin band surrounding the fracture plane. In fact, the strengths were best predicted in ref.[38] using the model in ref. [41], which predicts failure to occur from a doublet where the second fiber fracture is influenced by the stress concentration from the first fiber break. More recently, the strengths predicted using the model in ref.[41] also agreed extremely well with the measured strengths of single-ply TMCs with different fibers[42].

Finally, it may be noted that the current methodology is not restricted to metal matrix composites. It is equally well suited for polymer matrix systems, where there is the additional advantage of measuring *in situ* fiber stresses by optical scattering techniques.

CONCLUSIONS

(1) A method has been established for the single fiber fragmentation test in metal matrix composite system. The experimental technique relies on detection of fiber breaks by the acoustic emission technique, and on determination of fragment lengths using a novel ultrasonic SBR technique. The analysis is based on Curtin's fragmentation model, which accounts for the stochastic nature of fiber breaks.

(2) Results for the SCS-6 fiber show a high average shear stress under fragmentation conditions, well above that obtained by push-out testing.

(3) Microstructural observations show little, if any, evidence of a continuous shear crack along the interface. Rather, there is damage to the carbonaceous coating in the form radial cracks that start at the reaction zone and propagate radially through the coating and end next to the SiC surface. Also, there are small discontinuous shear cracks. The high average shear stress, τ, is consistent with the lack of evidence of any significant length of interface crack next to a fiber break, and is explained on the basis of a high clamping stress on the fiber immediately adjacent to a break.

(4) The *in situ* Weibull strength and modulus were low for the SCS-6 fibers compared with that obtained by testing individually extracted fibers. A possible reason is damage to the fibers, but the mechanism of damage has yet to be established.

(5) Multiple-fiber single-ply specimens show evidence of local load sharing even for weak interfaces. The combination of slip observations on the specimen faces, and SBR images of fiber breaks beneath the surface, illustrate a synergistic mechanism of localized matrix plasticity and fiber breakage. This mechanism of fiber breakage dominates over any interfacial effect, in contrast to conventional understanding of cumulative fiber fracture behavior. On a Weibull plot, the correlated fiber fractures manifest in a higher value of the *in situ* Weibull modulus.

ACKNOWLEDGEMENTS

This research was performed at the USAF Wright Laboratory Materials Directorate, Wright Patterson Air Force Base, through Contract numbers F 33615-91-C-5663 (BSM), F33615-96-C-5258 (BSM) and F-33615-94-C-5213 (TEM). Discussions with P. Karpur of the University of Dayton Research Institute, S.G. Warrier of UES, Inc., D. B. Gundel of Systran Corp., M.L. Gambone of the Materials Directorate, and the insightful comments of N. J. Pagano of the Materials Directorate, are sincerely acknowledged.

REFERENCES

1. Metcalfe, A.G., *Interfaces in Metal Matrix Composites*. Academic, New York, 1974.
2. Majumdar, B.S., Interfaces in metal matrix composites. In *Titanium Matrix Composites*, ed. S. Mall and T. Nicholas. Technomic Publications, Lancaster, PA, 1997, pp. 113–168.
3. Clyne, T.W., Feillard, P. and Kalton, A.F., Interfacial mechanics and macroscopic failure in titanium-based composites. ASTM Symposium on Life Prediction Methodology for Titanium Matrix Composites, Hilton Head, ASTM STP 1253, March 1994.
4. Ghosn, L.J., Eldridge, J.I. and Kantzos, P., Analytical modeling of the interfacial stress state during pushout testing of SCS-6/Ti-based composites. *Acta Metallurgica*, 1994, **42**(11), 3895–3908.
5. Warrier, S.G., Majumdar, B.S., Gundel, D.B. and Miracle, D.B., Implications of tangential shear failure during transverse loading of metal matrix composites. *Acta Metallurgica*, 1997, **45**(8), 3469–3480.
6. Miracle, D.B., Gundel, D.B. and Warrier, S.G., Interfacial structure and properties for the design of fiber-reinforced metal matrix

composites. In *Processing and Design Issues in High Temperature Materials*, ed. N.S. Stoloff and R.H. Jones. TMS, Warrendale, PA, 1996.
7. Koss, D.A., Kallas, M. N. and Hellman, J.R., Mechanics of interfacial failure during thinslice pushout tests. *MRS Symposium Proceedings*, 1992, **273**, 303–313.
8. Ghosn, L.J., Eldridge, J.I. and Kantzos, P., Analytical modeling of the interfacial stress state during pushout testing of SCS-6/Ti-based composites. *Acta Metallurgica*, 1994, **42**(11), 3895–3908.
9. Majumdar, B.S. and Miracle, D.B., Interface measurements and applications in fiber-reinforced MMCS. *Key Engineering Materials*, 1996, **116-117**, 153–172.
10. Kelly, A. and Tyson, W.R., *Journal of Mechanics and Physics of Solids*, 1965, **13**, 329–350.
11. Yavin, B., Gallis, H.E., Scherf, J., Eitan, A. and Wagner, H.D., Continuous monitoring of the fragmentation phenomenon in single fiber composite materials. *Polymer Composites*, 1991, **12**(6), 436–446.
12. Vassel, A., Merienne, M.C., Pautonnier, P., Molliex, L. and Favre, J.P. In *6th World Conference on Titanium*, ed. P. Lacombe, R. Tricot and G. Beranger, Les Editions de Physique, Les Ulis Cedex, France, 1988, pp. 919–923.
13. Le Petitcorps, Y., Pailler, R. and Naslain, R., *Composite Science and Technology*, 1989, **35**, 207–214.
14. Curtin, W.A., Exact theory of fiber fragmentation in a single-filament composite. *Journal of Material Science*, 1991, **26**, 5239–5253.
15. Matikas, T.E., Karpur, P. and Krishnamurthy, S., A non-destructive method for detecting and mapping of fiber fractures in metal matrix composites. *Composite Science and Technology*, 1997, **0**, 0.
16. Matikas, T.E. and Karpur, P., Ultrasonic reflectivity technique for the characterization of fiber–matrix interface in metal matrix composites. *Journal of Applied Physics*, 1993, **74**(1), 228–236.
17. Karpur, P., Matikas, T.E., Krishnamurthy, S. and Miracle, D.B., Recent developments in ultrasonic methods for metal matrix composites research. In *Proceedings of the 10th International Conference on Composite Materials*, ICCM-10, Vol. V, ed. A. Poursartip and K. Street, Woodhead Publishing Limited, 1995, pp. 479–486.
18. Drzal, L.T., Rich, M.J. and Lloyd, P.F., *Journal of Adhesion*, 1982, **16**, 1–30.
19. Gambone, M.L. and Wawner, F.E., The effect of elevated temperature exposure of composites on the strength distribution of the reinforcing fibers. *Material Resource Society Proceedings*, 1994, **350**, 111–118.
20. Gambone, M.L., SiC fiber strength after consolidation and heat treatment in Ti-23Al-23Nb matrix composite. *Scripta Metallurgica*, 1996, **34**(3), 507–512.
21. Ananth, C.R. and Chandra, N., Numerical modeling of fiber push-out test in metallic and intermetallic matrix composites-mechanics of the failure process. *Journal of Composite Materials*, 1995, **29**(2), 1488–1514.
22. Liang, C. and Hutchinson, J.W., Mechanics of the fiber pushout test. *Mechanics of Materials*, 1993, **14**, 207–221.
23. Yang, C.J., Jeng, S.M. and Yang, J.M., Interfacial properties measurement for SiC fiber-reinforced titanium alloy composites. *Scripta Metallurgica*, 1990, **24**, 469–474.
24. Gundel, D.B., Majumdar, B.S. and Miracle, D.B., Evaluation of the intrinsic transverse response of fiber-reinforced composites using a cross-shaped sample geometry. *Scripta Metallurgica*, 1995, **33**, 2057.
25. Gundel, D.B., Majumdar, B.S. and Miracle, D.B., The intrinsic transverse response of several SiC/Ti-6Al-4V composites to transverse tension, *Proceedings of ICCM-10*, Vol. 2, ed. A. Poursartip and K. Street, 1995, pp. 703–710.
26. Ning, X.J. and Pirouz, P., The microstructure of SCS-6 SiC fiber. *Journal of Material Resources*, 1991, **6**(10), 2234–2248.
27. Morscher, G., Pirouz, P. and Heuer, A.H., *Journal of the American Ceramic Society*, 1990, **73**, 713.
28. Lerch, B.A., Hull, D.R. and Leonhardt, T.A., *As Received Microstructure of a SiC/Ti-15-3 Composite*. NASA Tech. Publication, no. 100938, NASA Lewis Research Center, 1988.
29. Majumdar, B.S. and Newaz, G.M., Inelastic deformation of metal matrix composites: plasticity and damage mechanisms. *Philosophy Magazine*, 1992, **66**(2), 187–212.
30. Johnson, W.S., Lubowinski, S.J. and Highsmith, A.L., Mechanical characterization of unnotched SCS-6/Ti-15-3 MMC at room temperature, ASTM STP 1080, 1990, p. 193.
31. He, M.Y. and Hutchinson, J.W., Kinking of a crack out of an interface. *ASME Journal of Applied Mechanics*, 1989, **56**, 270–278.
32. Ebert, L.J. and Wright, P.K., Mechanical aspects of the interface. In *Interfaces in Metal Matrix Composites*, ed. A.G. Metcalfe. Academic, New York, 1974, pp. 30–63.
33. Wu, W., Desaeger, M., Verpost, I. and Varna, J., *Composite Science and Technology*, 1997, **57**, 809–819.
34. Nicholas, T. and Ahmad, J.A., Modeling fiber breakage in a metal–matrix composite. *Composite Science and Technology*, 1994, **52**, 29–38.
35. Carara, A.S. and McGarry, F.J., *Journal of Composite Materials*, 1968, **2**, 222.
36. Zok, F.W., Chen, X. and Weberl, C.H., Tensile strength of SiC fibers. *Journal of the American Ceramic Society*, 1995, **78**, 1965–1968.
37. He, M.Y., Evans, A.G. and Curtin, W.A., The ultimate tensile strength of metal and ceramic–matrix composites. *Acta Metallurgica*, 1993, **41**(3), 871–878.
38. Boehlert, C.J., Majumdar, B.S., Krishnamurthy, S. and Miracle, D.B., Role of matrix microstructure on RT tensile properties and fiber-strength utilization of an orthorhombic Ti-alloy based composite. *Metallurgy Transactions*, 1997, **28A**, 309–323.
39. Gundel, D.B. and Wawner, F.W., Experimental and theoretical investigation of the tensile strength of SiC/Ti-alloy composites. *Composite Science and Technology*, 1997, **57**, 471–481.
40. Curtin, W.A., Ultimate strengths of fiber-reinforced ceramics and metals. *Composites*, 1993, **24**, 98–102.
41. Zweben, C. and Rosen, B.W., A statistical theory of material strength with application to composite materials. *Journal of Mechanics and Physics of Solids*, 1970, **18**, 189–206.
42. Majumdar, B.S., Matikas, T.E. and Miracle, D.B., Effects of the interface on local versus global load sharing behavior in metal matrix composites under longitudinal loading. In *Proceedings of the International Conference on Composite Materials*, ICCM-11, Australia, August 1997.